Fluorination Enhanced Surface Stability of Disordered Rocksalt Cathodes

Linze Li[1+], Juhyeon Ahn[2+], Yuan Yue[2], Wei Tong[2], Guoying Chen[2], and Chongmin Wang[1]**

1. Environmental Molecular Sciences Laboratory, Pacific Northwest National Laboratory, 902 Battelle Boulevard, Richland, WA 99354, USA

2. Energy Storage and Distributed Resources Division, Lawrence Berkeley National Laboratory, 1 Cyclotron Road, Berkeley, CA 94720, USA

+These authors contributed equally to this work.

*To whom correspondence may be addressed.

Email: gchen@lbl.gov, chongmin.wang@pnnl.gov

ABSTRACT

Cation-disordered rocksalt (DRX) oxides are a promising new class of high-energy-density cathode materials for next-generation Li-ion batteries. However, their capacity fade during cycling presents a major challenge. Partial fluorine (F) substitution into oxygen (O) lattice appears to be an effective strategy for improving the cycling stability, but the underlying atomistic mechanism remains elusive. Here, using a combination of advanced transmission electron microscopy-based imaging and spectroscopy techniques, we probe the structural and chemical evolutions upon cycling of Mn-based DRX cathodes with an increasing F content (Li-Mn-Nb-O-F_x, x = 0, 0.05, 0.2). We reveal atomic origin behind the beneficial effect of high-level fluorination for enhancing surface stability of DRX. We discover that, due to the reduced O redox activity while with increasing F concentration, F in the DRX lattice mitigates the formation of O deficient surface layer upon cycling. For low F-substituted DRX, the O loss near the surface results in the formation of an amorphous cathode-electrolyte interphase layer and nanoscale voids after extended cycling. Increased F concentration in DRX lattice minimizes both O loss and the interfacial reactions between DRX and liquid electrolyte, enhancing surface stability of DRX. Our results provide guidance on development of next-generation cathode materials through anion substitution.

1. Introduction

With the fast advancement of energy storage technology based on Li-ion batteries (LIBs), the development of cobalt (Co) and nickel (Ni)-free cathode materials to replace the current nickel-manganese-cobalt (NMC)-based layered cathode materials becomes increasingly important for resolving the Co and Ni resource issue and meeting the rapidly growing demands of clean energy.[1] Among various candidates, cation-disordered rocksalts (DRX) have recently emerged as a new class of high-energy-density cathode materials that do not rely on Co or Ni and can be synthesized from a broad range of transition metals (TMs), particularly those earth-abundant ones, *e.g.*, iron (Fe), manganese (Mn), and titanium (Ti).[2] Intense research of DRX cathode materials over the past years has created a large number of novel DRX oxides, including $Li_{1.211}Mo_{0.467}Cr_{0.3}O_2$,[2a] $Li_{1.2}Mn_{0.4}Ti_{0.4}O_2$,[3] $Li_{1.3}Mn_{0.4}Nb_{0.3}O_2$,[4] $Li_{1.2}Mn_{0.6}Nb_{0.2}O_2$,[5] $Li_{1.25}Mn_{0.5}Nb_{0.25}O_2$,[6] $LiFe_{0.5}V_{0.5}O_2$,[7] $Li_{1.25}Nb_{0.25}V_{0.5}O_2$,[8] and $Li_{1.2}Mn_{0.2}V_{0.6}O_2$.[9]. In these DRX oxide cathodes, a Li-excess chemical composition is necessary to facilitate a three-dimensional (3D) Li percolation network for facile Li-ion transport in the DRX lattice.[2a, 10] Such Li-excess composition constrains the content of redox-active TM in the DRX compound and also enables oxygen (O) redox during the electrochemical process.[11] The O redox is much less reversible compared to TM redox, and a high level of O redox activity in the DRX oxides usually triggers significant O loss from the crystal lattice, and consequently, severe capacity fade after cycling.[4, 11-12] By using fluorine anion (F^-) substitution for oxygen anion (O^{2-}), fluorination can increase the amount of low-valence redox-active TM without sacrificing Li content in the DRX compound.[12a] Correspondingly, the increased TM redox capacity accommodated upon fluorination reduces the capacity reliability on O redox and thus mitigates irreversible O loss.[2b, 5, 9, 12a, 13] Due to the presence of local TM-poor, Li-rich environments in the DRX lattice that are highly favorable for F^-,[13-14] substantial levels of fluorine (F) substitution have been achieved in various DRX materials, such as Li_2VO_2F,[15] $Li_{1.2}Mn_{0.7}Nb_{0.1}O_{1.8}F_{0.2}$,[5],23 $Li_{1.2}Mn_{0.75}Nb_{0.05}O_{1.7}F_{0.3}$,[16] $Li_{1.2}Mn_{0.625}Nb_{0.175}O_{1.325}F_{0.675}$,[17] $Li_2Mn_{2/3}Nb_{1/3}O_2F$,[2b] $Li_{1.2}Ti_{0.2}Mn_{0.6}O_{1.8}F_{0.2}$,[18] and Li_2MoO_2F.[19] In general, fluorination has been demonstrated as a very effective route for improving the cycling stability in all these fluorinated DRX (F-DRX) cathodes.

In a previous work based on electrochemical measurements and X-ray absorption spectroscopy (XAS), it was proposed that cycling-induced performance degradation in a

$Li_{1.3}Nb_{0.3}Mn_{0.4}O_2$ DRX cathode is likely due to densification of TMs near the surface and thus reduced quality of the local Li percolation network.[12b] Furthermore, using scanning transmission electron microscopy (STEM), we previously discovered that in a $Li_{1.2}Ti_{0.4}Mn_{0.4}O_2$ DRX cathode, extensive cycling results in a high level of structural degradation including amorphization and void formation at the particle surface, which impedes Li transport and causes fast capacity loss; while in a highly fluorinated $Li_{1.2}Ti_{0.2}Mn_{0.6}O_{1.8}F_{0.2}$ DRX cathode, the cycling-induced surface degradation is much less prominent, and the cycling stability is greatly improved.[18] These previous studies indicate that the chemical and structural stability near the surface of DRX cathode materials plays a critical role in determining the cycling performance. However, a detailed understanding of the cycling-induced chemical reconstruction and TM oxidation states evolution associated with the structural evolution near the surface of the DRX cathodes remains elusive. Particularly, the formation of cathode-electrolyte interface (CEI) layer at the surface of DRX cathode has not been directly observed in previous studies, and the effects of fluorination on CEI layers remains elusive.

Here, using a combination of STEM, high-resolution transmission electron microscopy (HRTEM), energy-dispersive X-ray spectroscopy (EDS), and electron energy loss spectroscopy (EELS) techniques, we systematically investigated nanoscale structure, chemistry, and valence changes after cycling of a series of Mn-based DRX cathodes, $Li_{1.2}Mn_{0.6+x/2}Nb_{0.2-x/2}O_{2.0-x}F_x$ ($LMNOF_x$, x = 0, 0.05, and 0.2). We show that, for the $LMNOF_x$ cathodes with no or low F concentration (x = 0 and 0.05, which are denoted as $LMNOF_0$ and $LMNOF_{0.05}$, respectively), the repeated charging and discharging processes lead to a degraded surface that has two sublayers – a nanoscale amorphous CEI layer on the outmost surface and an O deficient layer at the inner surface, as well as void formation resulted from severe elemental loss at the subsurface region, all of which degrade the Li transport properties. In contrast, for the $LMNOF_x$ cathodes with a high F concentration (x = 0.2, denoted as $LMNOF_{0.2}$), the crystal structure and chemical distribution near the surface is well preserved after cycling with almost no amorphous CEI layer or void structures formed, which ensures facile Li transport. These results not only advance the fundamental understanding of the beneficial effects of increasing the F concentration in the DRX lattice for mitigating cycling induced surface structural degradation, but also provide useful insights into the design of novel cathode materials with improved cycling stability.

2. Results and Discussion

2.1 Electrochemical Properties

$LMNOF_x$ cathode materials were synthesized using a solid-state synthesis route as described in our previous work.[16] The phase-pure cubic disordered rocksalt structures with a $Fm\bar{3}m$ symmetry were confirmed by the XRD patterns collected on the bulk powder samples (Figure S1, Supporting Information). The stoichiometries were close to the target chemical compositions measured by inductively coupled plasma (ICP) spectroscopy and F ion selective electrode measurements (ISE) (Table S1, Supporting Information). Before the electrochemical tests, the as-synthesized powders were blended with carbon additives via a mechanochemical process. The resulting particles are mostly within a few hundreds of nanometers to a few microns in size, as shown by the TEM images (Figure S2, Supporting Information). The cation (Mn and Nb) and anion (O and F) elements are uniformly distributed at the particle level in all the pristine particles as confirmed by the STEM images and corresponding EDS elemental maps (Figure S3-S5, Supporting Information). Following the cycling process, the sizes and morphologies of the particles did not change obviously (Figure S2, Supporting Information), and the elemental distribution remained uniform at the particle level (Figure S3-S5, Supporting Information).

Electrochemical performance evaluation shows reduced O redox activity with increasing F substitution in the $LMNOF_x$ system, as shown by the voltage and the corresponding dQ/dV profiles where reduced voltage plateau and the oxidation peak intensity were observed at the high voltage region at about 4.5 V in high-F DRX (Figure S6a,b, Supporting Information). In $LMNOF_0$, large O redox contribution was observed initially, however, it faded quickly over cycling, clearly shown in Figure 1a,b. Although a small amount of F substitution in $LMNOF_{0.05}$ reduced the O redox participation to some extent, the irreversibility remained (Figure1c,d). As a result, the capacity retentions for $LMNOF_0$ and $LMNOF_{0.05}$ were about 84% and 91% after 30 cycles, respectively (Figure S6c, Supporting Information). By increasing F content considerably, O redox peak nearly disappeared and better reversibility was achieved on $LMNOF_{0.2}$ (Figure 1e,f). Because of the considerably reduced O redox contribution, the capacity is lower than those of $LMNOF_0$

and $LMNOF_{0.05}$ in the initial cycle, yet, it is much stable over cycling. It should be pointed out, for the initial cycle, when cycling DRX cathodes to 4.8 V, processes involving Mn redox, O redox, O_2 release and side reactions with the electrolyte all contribute to the 1st cycle charge capacity. We observed that all the three cathodes have similar 1st cycle charge capacities (Figure 1). Upon discharge, the main capacity contributors are considered to be Mn redox and O redox. We observed that $LMNOF_{0.2}$ has much less 1st cycle discharge capacity compared to the other two cathodes of less F or F-free (Figure 1 and Figure S6c, Supporting Information). The reduced 1st cycle discharge capacity of the $LMNOF_{0.2}$ cathode is the major reason for its pronounced capacity discrepancy of the charge and discharge capacities in the 1st cycle. This appears to be caused by the effect of fluorination, as it has been shown that fluorination may reduce the amount of Li atoms in the Li-percolation network of the DRX lattice and thus reduce the capacity.[14]

2.2. Atomic Level Structural and Chemical Evolution Upon Cycling

To explore the cycling-induced atomic structure evolution near the cathode surface, HRTEM images were collected for the pristine and cycled $LMNOF_0$ particles, which are shown in Figure 2a and b, respectively. While the surface structure of the pristine $LMNOF_0$ particle is mostly crystalline, an amorphous layer of ~5 nm is observed at the particle surface after the extensive cycling, indicating cycling-induced surface structural degradation. The formation of amorphous surface layers has been observed at different local regions in different cycled $LMNOF_0$ particles (Figure S7, Supporting Information). Along with this finding, the cycling-induced chemical changes were examined through the EDS linescan measured profiles of atomic-percentage compositions from the surface to the bulk in the pristine and the cycled $LMNOF_0$ particles (Figure 2c,d). In addition to measuring Mn, Nb, and O, which are the dominating elements of the $LMNOF_0$ cathode, F and P were also concurrently measured, because they are indicators for the formation of surface CEI layers such as $Li_xPO_yF_z$.[20] The measurements show that non-uniform elemental distribution is generally restricted to the surface or near-surface regions for both the pristine and cycled $LMNOF_0$ particles. In the pristine $LMNOF_0$ particle (Figure 2c), while the Nb distribution is mostly uniform from the bulk to the surface, there is a thin (3 nm) O-deficient and Mn-rich surface layer. Similarly, O-deficient surface layers in pristine DRX cathodes have also been observed in our previous study of Li-Mn-Ti-O DRX cathodes,[18] indicating that the surface O loss

might be a common phenomenon during the preparation of DRX cathode materials, where high calcination temperature and inert atmosphere are involved.

In the cycled $LMNOF_0$ particle, the chemical distribution near the surface is more complicated (Figure 2d). In particular, the O-deficient surface area in the cycled particle is much thicker (12 nm) compared to that (3 nm) in the pristine particle, and this surface area can be further divided into two layers: (1) a 5-nm-thick outmost surface layer (OSL) and (2) a 7-nm-thick inner surface layer (ISL) (Figure 2d). Compared to the bulk composition of the cycled particle, the OSL shows dramatically reduced concentration of TMs, but greatly increased concentration of F and P. Therefore, it is considered as a CEI layer generated during the cycling. This CEI-related OSL corresponding to the region (1) in Figure 2b is largely amorphous in nature, as confirmed by the fast Fourie transform (FFT) pattern of the local region. In the ISL, there are only slightly increased F and P concentrations, with no obvious difference in TM concentration as compared to the bulk. This ISL corresponding to the region (2) in Figure 2b is mostly in the form of crystalline DRX structures, and thus should be regarded as an O-deficient surface layer in the cycled DRX particle. The F and P enrichment at the cathode surface could partially be a result of the decomposition of the electrolyte and its side reaction with the cathode materials. The thickness of the O-deficient ISL in the cycled particle (7 nm) is larger than that in the pristine particle (3 nm), which is believed to be caused by irreversible O release at the surface during the cycling process, as observed in many other DRX oxides.[5, 12a, 18]

The cycling-induced chemical evolution in the $LMNOF_0$ cathode particles was further investigated by STEM imaging and EELS mapping. STEM high-angle annular dark-field (HAADF) images and corresponding EELS maps of the O *K*, Mn *L*, and Li *K* edges for the pristine and cycled $LMNOF_0$ particles are shown in Figure 3a and b, respectively. For the pristine $LMNOF_0$ (Figure 3a), the observed intensity distribution in the STEM HAADF image and EELS maps indicate that the cations and anions are mostly uniformly distributed in the particle except for a small amount of Li loss near the particle surface. In comparison, for the cycled $LMNOF_0$, a high density of black-dot-like nanoregions are observed in the STEM HAADF image (Figure 3b). The corresponding EELS elemental maps show that these black-dot-like nanoregions should be void structures with local material loss, similar to those previously observed in Li-rich layered[21] and disordered[18] rocksalt structured cathodes. In those cathodes, it is believed that the O redox activity

during the electrochemical cycling facilitates the O migration from the bulk lattice towards surface, while O vacancies are injected to the surface and penetrated into the bulk.[18, 21] It should be also noted that voids are often seen to be formed in layer-structured NMC cathodes during the cycling,[22] the origin of which has been recently identified as a consequence of cycling-induced accumulation of intrinsically existing vacancies dispersed in the bulk of the cathode.[23] In the present case of the $LMNOF_0$ cathode, we believe that the mechanism of surface O vacancy injection should operate to boost the void formation due to the high-level of O redox participation from the initial cycling (Figure 1a,b). Loss of a significant amount of Li is observed at the voids and at local nanoregions near the voids (Figure 3b), which should deteriorate Li transport from the surface area to the bulk, leading to the capacity drop upon cycling.

2.3. Electronic Structure and Spatial Distribution of Oxygen

EELS mapping can also directly visualize the distribution of Mn oxidation states near the surface, as the reduction of the Mn valence can be reflected by the shift of the Mn L_3 peak to lower energies.[24] The mapped energy shifts (ΔE) of the Mn L_3 peaks near the surface for the pristine and cycled $LMNOF_{0.0}$ particles, with respect to the energy position measured in the bulk areas (where ΔE is defined as 0 eV), are shown in Figure 3c,d, respectively. In the pristine $LMNOF_0$ particle (Figure 3c), while the average Mn oxidation state remains trivalent in the bulk powder, a distinct energy shift of the Mn L_3 peaks (ΔE = -1.94 eV) is observed within a thin surface layer (~ 5 nm), indicating that the reduction of Mn valence is inherently present at the surface that is O deficient. On the other hand, in the cycled $LMNOF_0$ particle (Figure 3d), there is a much stronger gradient distribution for the energy shifts of the Mn L_3 peaks from the bulk to the surface (ΔE = -1.84 eV), indicating that the Mn valence reduction penetrates much deeper area (up to 35 nm). Since the Mn valence reduction can compensate for O loss, such observed cycling-induced changes of the Mn valence distribution indeed suggest that O loss is severe after cycling consistent with the EDS results (Figure 2c,d).

Comparable characterization and analysis were also performed on the $LMNOF_{0.05}$ and $LMNOF_{0.2}$ cathode particles. In general, the pristine and cycled $LMNOF_{0.05}$ particles (Figure 4 and Figure 5) show remarkably similar characteristics as compared to those pristine and cycled $LMNOF_0$ particles (Figure 2 and Figure 3), respectively. These characteristics include ***i)*** crystalline

surface structures in the pristine $LMNOF_{0.05}$ particle, and an about 5-nm-thick amorphous surface layer in the cycled one, as shown by the HRTEM images in Figure 4a,b; ***ii)*** a 3-nm-thick surface layer that is O-deficient and Mn-rich in the pristine particle, and a dual-surface-layer structure in the cycled one: (1) a 5-nm-thick CEI OSL layer with reduced concentration of TMs but increased concentration of F and P, followed by (2) a 7-nm-thick O-deficient ISL, as revealed by the STEM EDS linescan profiles in Figure 4c,d; ***iii)*** uniform elemental distribution in the pristine particle, and formation of nanoscale voids in the cycled one, as shown by the STEM HAADF images and corresponding EELS maps in Figure 5a,b; and ***iv)*** a thin surface layer showing Mn valence reduction (ΔE = -0.87 eV) in the pristine particle, and a much deeper region showing gradient distribution of Mn valences from the surface to the bulk (ΔE = -1.71 eV) in the cycled one, as revealed by the maps of the Mn L_3 peak energy shifts in Figure 5c,d. Compared to the cycled $LMNOF_0$ particle (Figure 3b), the loss of Mn, O, and Li in the cycled $LMNOF_{0.05}$ particle (Figure 5b) appears to be less severe, indicating that a small amount of F substitution of O in the DRX lattice is beneficial to the structural stability, although it is insufficient to fully prevent the elemental loss during the electrochemical cycling (Figure 5b).

Further increasing the F concentration to a high level in the DRX lattice can improve the structural stability dramatically, which is confirmed by our characterizations of the $LMNOF_{0.2}$ cathode particles (Figure 6 and Figure 7). The HRTEM images show that, unlike the $LMNOF_{0.0}$ and $LMNOF_{0.05}$ particles, which developed nanoscale surface amorphous layers after cycling (Figure 2b,4b, and Figure S7a,b, Supporting Information), the $LMNOF_{0.2}$ particle mostly maintained the crystalline surface structure even after extended cycling (Figure 6b and Figure S7c, Supporting Information). Correspondingly, STEM EDS linescan measurements in Figure 6c,d show that the concentration variation (a decrease in TM but an increase in P) in the O deficient surface layer is strongly suppressed in the cycled $LMNOF_{0.2}$ particle. EELS linescan measurements further confirms that O loss at the particle surface can be greatly mitigated in the cycled $LMNOF_{0.2}$ particle (Figure 8). These results suggest that in the $LMNOF_{0.2}$ cathode, the formation of amorphous surface CEI layers after the cycling is mostly suppressed with largely reduced O redox activity. Further, the STEM HAADF images and corresponding EELS maps in Figure 7a,b confirm that the uniform elemental distribution is maintained after the cycling. The maps of the Mn L_3 peak energy shifts in Figure 7c,d show that in both the pristine and cycled $LMNOF_{0.2}$ particles the Mn valence reduction mostly occurs at the thin (~ 5 nm) surface layers

corresponding to the local O loss, which is consistent with the EDS measurements (Figure 6c,d). Most importantly, the well-preserved Li distribution can ensure facile Li-ion diffusion at the surface of the $LMNOF_{0.2}$ cathode after cycling. These findings clearly demonstrate the critical role of high-level fluorination in the DRX cathode for the greatly enhanced structural stability and chemical homogeneity during cycling. It should be noted that for the practical application, we will need to further demonstrate the long-term material stability associated with the chemical/structural changes induced not only by the O redox but also by the Mn redox reversibility at the surface and in the bulk of the cathode particles. Apparently, such a demonstration of long-term cycling stability requires further systematic study that is in progress and will be reported in a follow up paper.

To sum up, schematics for the comparison of the cycling-induced structural and chemical evolutions in the $LMNOF_0$, $LMNOF_{0.05}$, and $LMNOF_{0.2}$ cathodes are depicted in Figure 9. By using fluorine anion (F^-) substitution for oxygen anion (O^{2-}), fluorination can increase the amount of low-valence redox-active TM without sacrificing Li content in the DRX compound.[9, 12a, 13] Here, the high-F-concentration compound $LMNOF_{0.2}$ has more redox-active Mn than the F-free compound $LMNOF_0$ and low-F-concentration compound $LMNOF_{0.05}$. Upon cycling, charge compensation in $LMNOF_{0.2}$ relies more on Mn redox contribution and less on O redox, and thus $LMNOF_{0.2}$ has less irreversible O loss. Our observations suggest that the amorphous CEI layer on the outmost surface and the nanoscale voids dispersed within the subsurface area are correlated to O redox that largely participates in the cycling process. By efficiently suppressing the O redox activity through a high level of F substitution, these unfavorable surface degradations detrimental to the Li transport are strongly mitigated.

3. Conclusion

With a combination of HRTEM, STEM, EDS, and EELS measurements, we show that, during the electrochemical cycling process, the structural stability of the $LMNOF_{0.2}$ cathode with high-level fluorination is greatly enhanced as compared with those of the $LMNOF_{0.0}$ and $LMNOF_{0.05}$ cathodes with zero or low-level fluorination. This is evidenced by the dramatically diminished amorphous CEI layers on the outmost surface, better preserved crystalline structures at the inner surface, and less disrupted chemical distributions at the subsurface of the $LMNOF_{0.2}$ cathode particles, as compared to those chemical and structural features in the $LMNOF_{0.0}$ and

$LMNOF_{0.05}$ particles. These observations spotlight the critical beneficial role of high-level fluorination on mitigating the drawbacks of irreversible oxygen redox activity and improving the structural stability of the DRX cathodes. Our results provide insights to constructive approach of anion substitution for improving the surface stability of cathode materials. The present study is of importance for understanding the correlation of the structural and chemical features to the electrochemical performances of cathode materials.

Supporting Information
Supporting Information is available from the Wiley Online Library or from the author.

Acknowledgments

This work was supported by the Assistant Secretary for Energy Efficiency and Renewable Energy, Vehicle Technologies Office, of the U.S. Department of Energy under Contract No. DEAC02-05CH11231 and DE-LC-000L053 under the program of Next Generation Cathode. Part of the work was conducted at the William R. Wiley Environmental Molecular Sciences Laboratory (EMSL), a national scientific user facility sponsored by DOE's Office of Biological and Environmental Research and located at PNNL. PNNL is operated by Battelle for the Department of Energy under Contract DE-AC05-76RLO1830.

Conflict of Interest
The authors declare no conflict of interest.

Data Availability Statement
The data that support the findings of this study are available from the corresponding author upon reasonable request.

Keywords
Disordered rocksalt, cathode, fluorene substitution, lattice stability, oxygen loss, cycling stability

References

[1] a) C. P. Grey, D. S. Hall, *Nat. Commun.* **2020**, 11, 6279; b) A. Masias, J. Marcicki, W. A. Paxton, *ACS Energy Lett.* **2021**, 6, 621; c) S. W. D. Gourley, T. Or, Z. W. Chen, *Iscience* **2020**, 23, 101505; d) C. Xu, Q. Dai, L. Gaines, M. Hu, A. Tukker, B. Steubing, *Commun. Mater.* **2020**, 1, 99.

[2] a) J. Lee, A. Urban, X. Li, D. Su, G. Hautier, G. Ceder, *Science* **2014**, 343, 519; b) J. Lee, D. A. Kitchaev, D. H. Kwon, C. W. Lee, J. K. Papp, Y. S. Liu, Z. Y. Lun, R. J. Clement, T. Shi, B. D. McCloskey, J. H. Guo, M. Balasubramanian, G. Ceder, *Nature* **2018**, 556, 185; c) R. J. Clement, Z. Lun, G. Ceder, *Energ. Environ. Sci.* **2020**, 13, 345; d) D. Chen, J. Ahn, G. Chen, *ACS Energy Lett.* **2021**, 6, 1358.

[3] N. Yabuuchi, M. Nakayama, M. Takeuchi, S. Komaba, Y. Hashimoto, T. Mukai, H. Shiiba, K. Sato, Y. Kobayashi, A. Nakao, M. Yonemura, K. Yamanaka, K. Mitsuhara, T. Ohta, *Nat. Commun.* **2016**, 7, 13814.
[4] N. Yabuuchi, M. Takeuchi, M. Nakayama, H. Shiiba, M. Ogawa, K. Nakayama, T. Ohta, D. Endo, T. Ozaki, T. Inamasu, K. Sato, S. Komaba, *P. Natl. Acad. Sci. USA* **2015**, 112, 7650.
[5] Z. Y. Lun, B. Ouyang, D. A. Kitchaev, R. J. Clement, J. K. Papp, M. Balasubramanian, Y. S. Tian, T. Lei, T. Shi, B. D. McCloskey, J. Lee, G. Ceder, *Adv. Energy Mater.* **2019**, 9, 1802959.
[6] M. A. Jones, P. J. Reeves, I. D. Seymour, M. J. Cliffe, S. E. Dutton, C. P. Grey, *Chem. Commun.* **2019**, 55, 9027.
[7] M. A. Cambaz, B. P. Vinayan, H. Euchner, S. A. Pervez, H. Gesswein, T. Braun, A. Gross, M. Fichtner, *ACS Appl. Mater. Inter.* **2019**, 11, 39848.
[8] M. Nakajima, N. Yabuuchi, *Chem. Mater.* **2017**, 29, 6927.
[9] D. A. Kitchaev, Z. Y. Lun, W. D. Richards, H. W. Ji, R. J. Clement, M. Balasubramanian, D. H. Kwon, K. H. Dai, J. K. Papp, T. Lei, B. D. McCloskey, W. L. Yang, J. Lee, G. Ceder, *Energy Environ. Sci.* **2018**, 11, 2159.
[10] A. Urban, J. Lee, G. Ceder, *Adv. Energy Mater.* **2014**, 4, 1400478.
[11] D. H. Seo, J. Lee, A. Urban, R. Malik, S. Kang, G. Ceder, *Nat. Chem.* **2016**, 8, 692.
[12] a) J. Y. Lee, J. K. Papp, R. J. Clement, S. Sallis, D. H. Kwon, T. Shi, W. L. Yang, B. D. McCloskey, G. Ceder, *Nat. Commun.* **2017**, 8, 981; b) D. C. Chen, W. H. Kan, G. Y. Chen, *Adv. Energy Mater.* **2019**, 9, 1901255.
[13] W. D. Richards, S. T. Dacek, D. A. Kitchaev, G. Ceder, *Adv. Energy Mater.* **2018**, 8, 1701533.
[14] B. Ouyang, N. Artrith, Z. Y. Lun, Z. Jadidi, D. A. Kitchaev, H. W. Ji, A. Urban, G. Ceder, *Adv. Energy Mater.* **2020**, 10, 1903240.
[15] R. Y. Chen, S. H. Ren, M. Knapp, D. Wang, R. Witter, M. Fichtner, H. Hahn, *Adv. Energy Mater.* **2015**, 5, 1401814.
[16] J. Ahn, D. Chen, G. Chen, *Adv. Energy Mater.* **2020**, 10, 2001671.
[17] Y. Yue, N. Li, Y. Ha, M. J. Crafton, B. D. McCloskey, W. Yang, W. Tong, *Adv. Func. Mater.* **2021**, 31, 2008696.
[18] L. Z. Li, Z. Y. Lun, D. C. Chen, Y. Yue, W. Tong, G. Y. Chen, G. Ceder, C. M. Wang, *Adv. Funct. Mater.* **2021**, 2101888.
[19] N. Takeda, S. Hoshino, L. Xie, S. Chen, I. Ikeuchi, R. Natsui, K. Nakura, N. Yabuuchi, *J. Power Sourc.* **2017**, 367, 122.
[20] W. Liu, J. X. Li, W. T. Li, H. Y. Xu, C. Zhang, X. P. Qiu, *Nat. Commun.* **2020**, 11, 3629.
[21] P. F. Yan, J. M. Zheng, Z. K. Tang, A. Devaraj, G. Y. Chen, K. Amine, J. G. Zhang, L. M. Liu, C. M. Wang, *Nat. Nanotech.* **2019**, 14, 602.
[22] a) C. S. Yoon, H. H. Ryu, G. T. Park, J. H. Kim, K. H. Kim, Y. K. Sun, *J. Mater. Chem. A* **2018**, 6, 4126; b) H. H. Ryu, K. J. Park, C. S. Yoon, Y. K. Sun, *Chem. Mater.* **2018**, 30, 1155; c) G. L. Xu, Q. Liu, K. K. S. Lau, Y. Liu, X. Liu, H. Gao, X. W. Zhou, M. H. Zhuang, Y. Ren, J. D. Li, M. H. Shao, M. G. Ouyang, F. Pan, Z. H. Chen, K. Amine, G. H. Chen, *Nat. Energy* **2019**, 4, 484.
[23] L. Li, J. Hu, J. Xiao, C. Wang, *ACS Appl. Mater. Inter.* **2021**, 13, 18849.
[24] a) S. L. Zhang, K. J. T. Livi, A. C. Gaillot, A. T. Stone, D. R. Veblen, *Am. Mineral.* **2010**, 95, 1741; b) C. D. Amos, M. A. Roldan, M. Varela, J. B. Goodenough, P. J. Ferreira,

Nano Lett. **2016**, 16, 2899; c) P. F. Yan, J. M. Zheng, X. F. Zhang, R. Xu, K. Amine, J. Xiao, J. G. Zhang, C. M. Wang, *Chem. Mater.* **2016**, 28, 857.

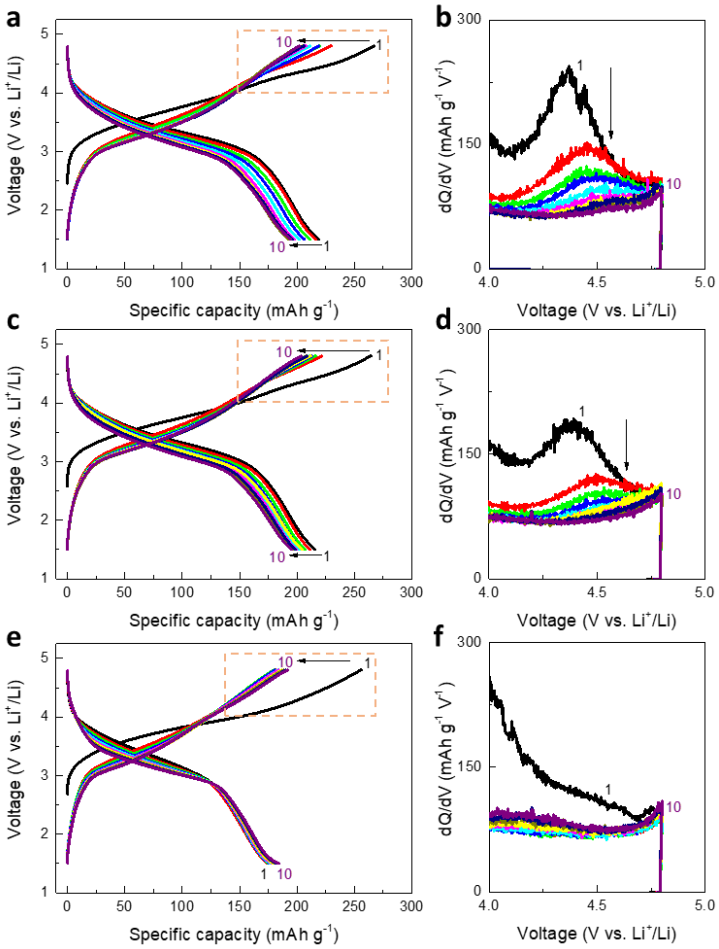

Figure 1. Electrochemical performances collected on the $LMNOF_x$ (x = 0, 0.05, and 0.2) cathodes. (a,c,e) voltage profiles and the (b,d,f) corresponding differential capacity versus voltage (dQ/dV) plots at a higher voltage region during the first 10 cycles for (a,b) $LMNOF_0$, (c,d) $LMNOF_{0.05}$, and (e,f) $LMNOF_{0.2}$. The black and purple lines indicate the 1st and the 10th cycles, respectively.

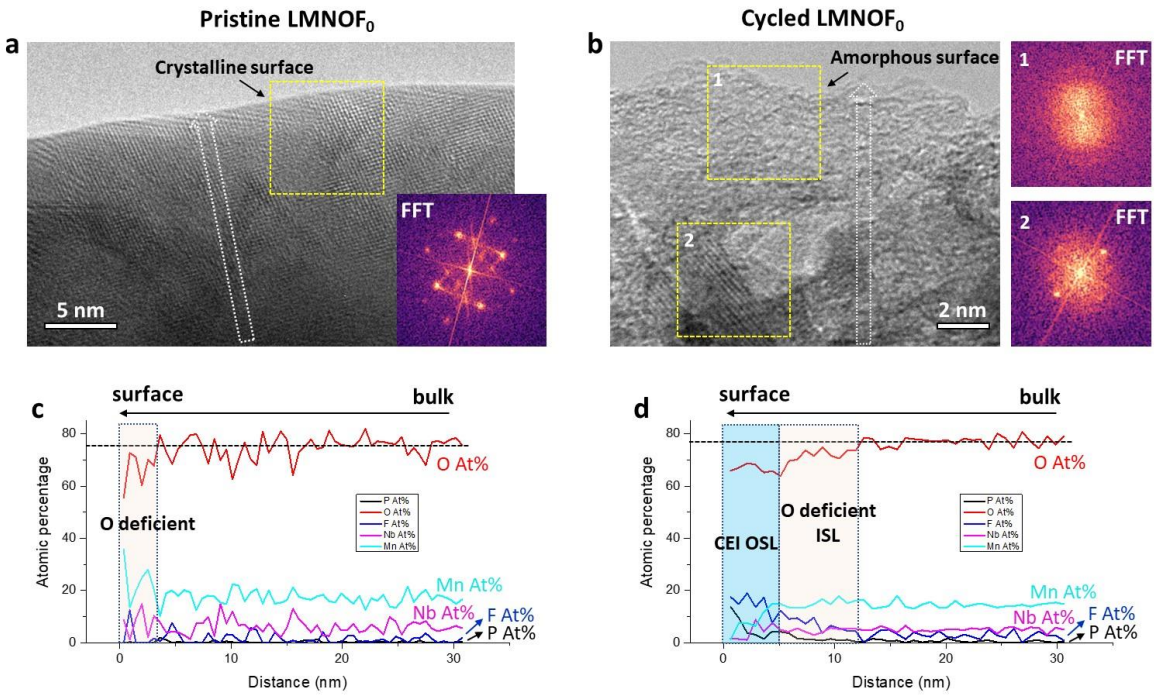

Figure 2. Cycling-induced structural and chemical evolution in $LMNOF_0$ cathode particles. (a, b) HRTEM images of nanoscale surface regions in a pristine particle (a) and a cycled particle (b). The insets show the fast Fourier transform (FFT) of the local regions highlighted by the yellow squares. The white arrows mark the linescan directions for the corresponding EDS measurements. (c, d) EDS linescan measurements showing the changes of the atomic percentage compositions from the bulk to the surface in the pristine particle (c) and the cycled particle (d).

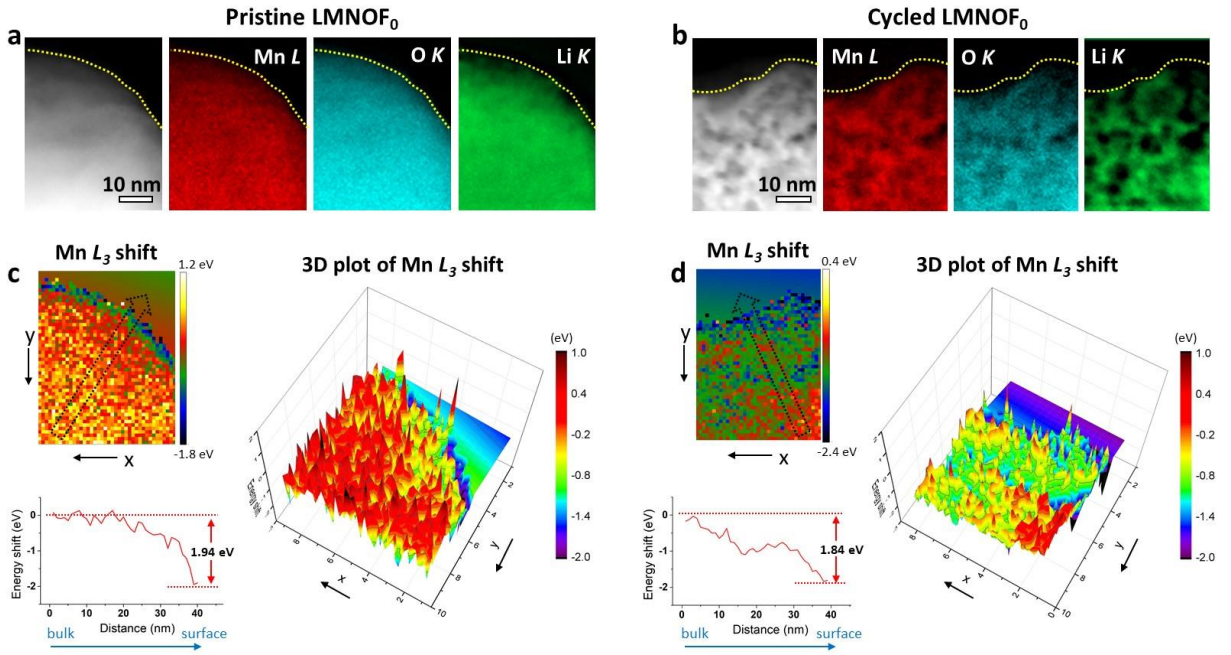

Figure 3. Cycling-induced chemical reconstruction and Mn oxidate states evolution in $LMNOF_0$ cathode particles. (a, b) STEM HAADF images and corresponding EELS maps of nanoscale surface regions in a pristine particle (a) and a cycled particle (b). (c, d) Corresponding color maps of the Mn L_3 peak energy shift for the pristine particle (c) and the cycled particle (d). The 2D maps have also been converted to 3D surface plots on the right side. Line profiles for the energy shifts measured along the direction marked by the black dashed arrows in the 2D maps are plotted at the bottom.

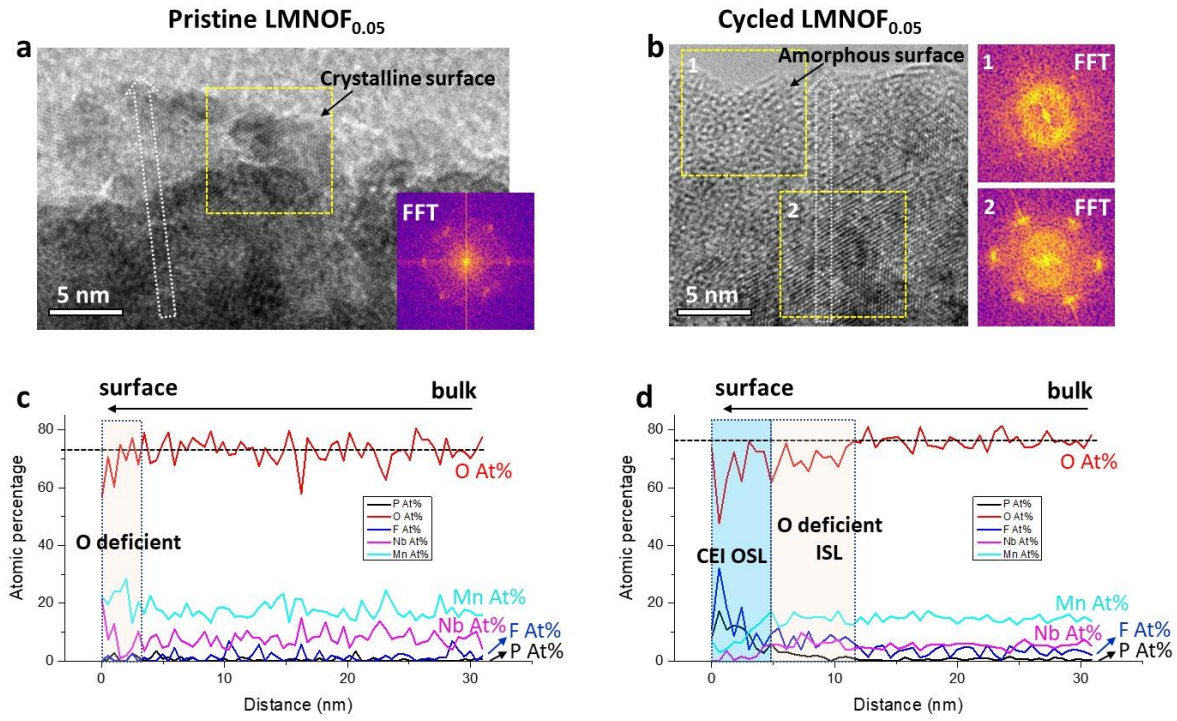

Figure 4. Cycling-induced structural and chemical evolution in $LMNOF_{0.05}$ cathode particles. (a, b) HRTEM images of nanoscale surface regions in a pristine particle (a) and a cycled particle (b). The insets show the fast Fourier transform (FFT) of the local regions highlighted by the yellow squares. The white arrows mark the linescan directions for the corresponding EDS measurements. (c, d) EDS linescan measurements showing the changes of the atomic percentage compositions from the bulk to the surface in the pristine particle (c) and the cycled particle (d).

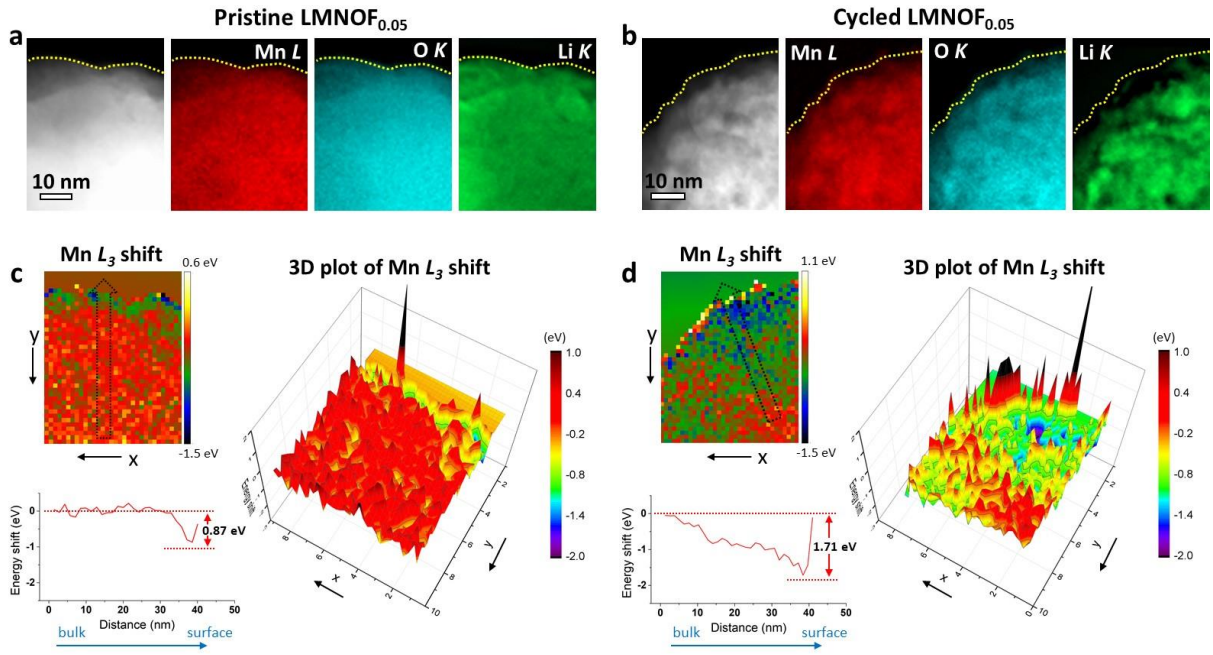

Figure 5. Cycling-induced chemical reconstruction and Mn oxidate states evolution in $LMNOF_{0.05}$ cathode particles. (a, b) STEM HAADF images and corresponding EELS maps of nanoscale surface regions in a pristine particle (a) and a cycled particle (b). (c, d) Corresponding color maps of the Mn L_3 peak energy shift for the pristine particle (c) and the cycled particle (d). The 2D maps have also been converted to 3D surface plots on the right side. Line profiles for the energy shifts measured along the direction marked by the black dashed arrows in the 2D maps are plotted at the bottom.

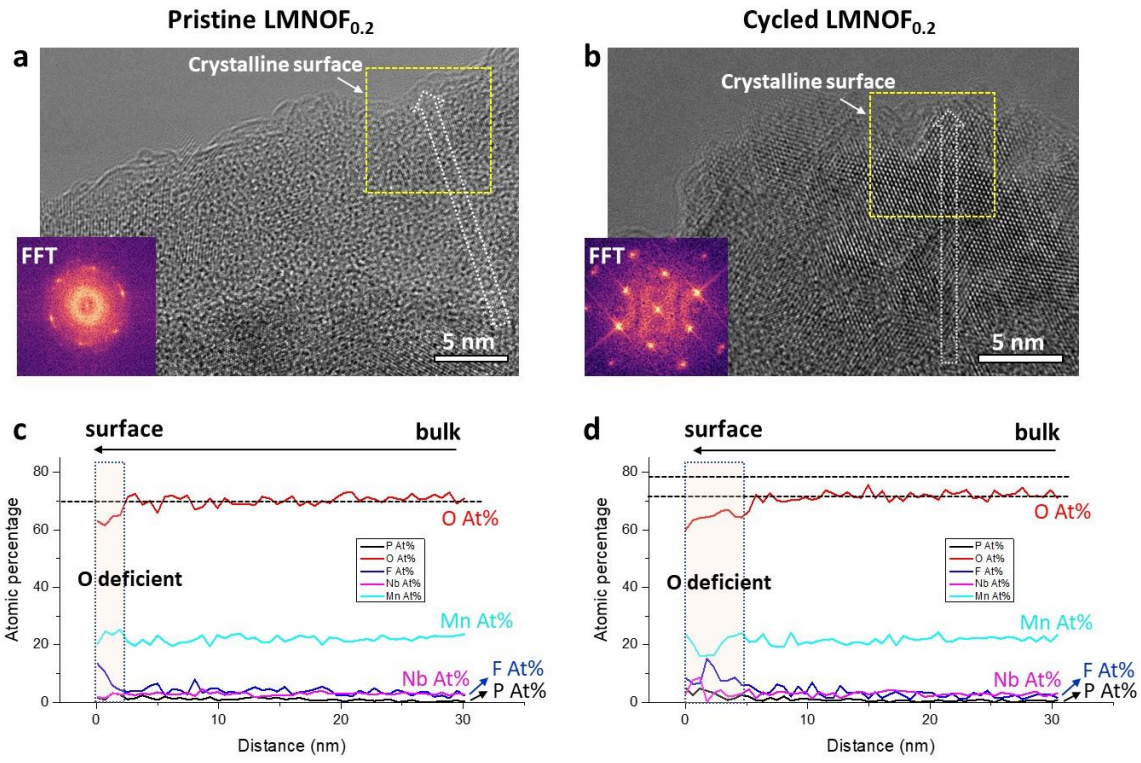

Figure 6. Cycling-induced structural and chemical evolution in $LMNOF_{0.2}$ cathode particles. (a, b) HRTEM images of nanoscale surface regions in a pristine particle (a) and a cycled particle (b). The insets show the fast Fourier transform (FFT) of the local regions highlighted by the yellow squares. The white arrows mark the linescan directions for the corresponding EDS measurements. (c, d) EDS linescan measurements showing the changes of the atomic percentage compositions from the bulk to the surface in the pristine particle (c) and the cycled particle (d).

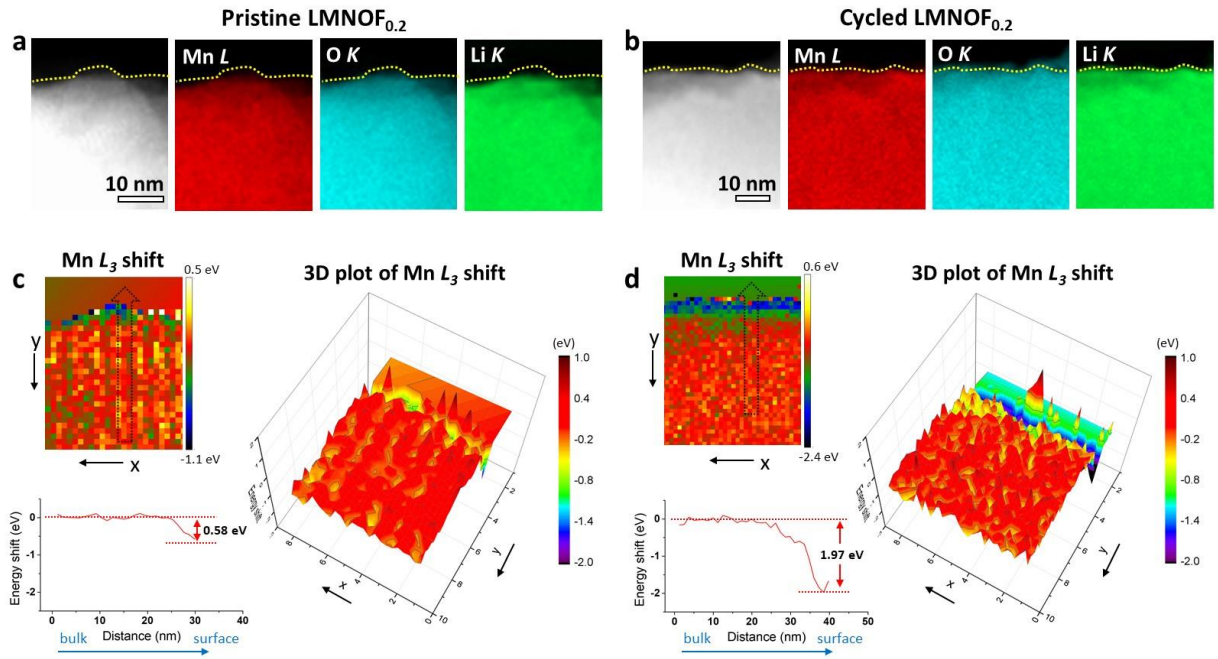

Figure 7. Cycling-induced chemical reconstruction and Mn oxidate states evolution in $LMNOF_{0.2}$ cathode particles. (a, b) STEM HAADF images and corresponding EELS maps of nanoscale surface regions in a pristine particle (a) and a cycled particle (b). (c, d) Corresponding color maps of the Mn L_3 peak energy shift for the pristine particle (c) and the cycled particle (d). The 2D maps have also been converted to 3D surface plots on the right side. Line profiles for the energy shifts measured along the direction marked by the black dashed arrows in the 2D maps are plotted at the bottom.

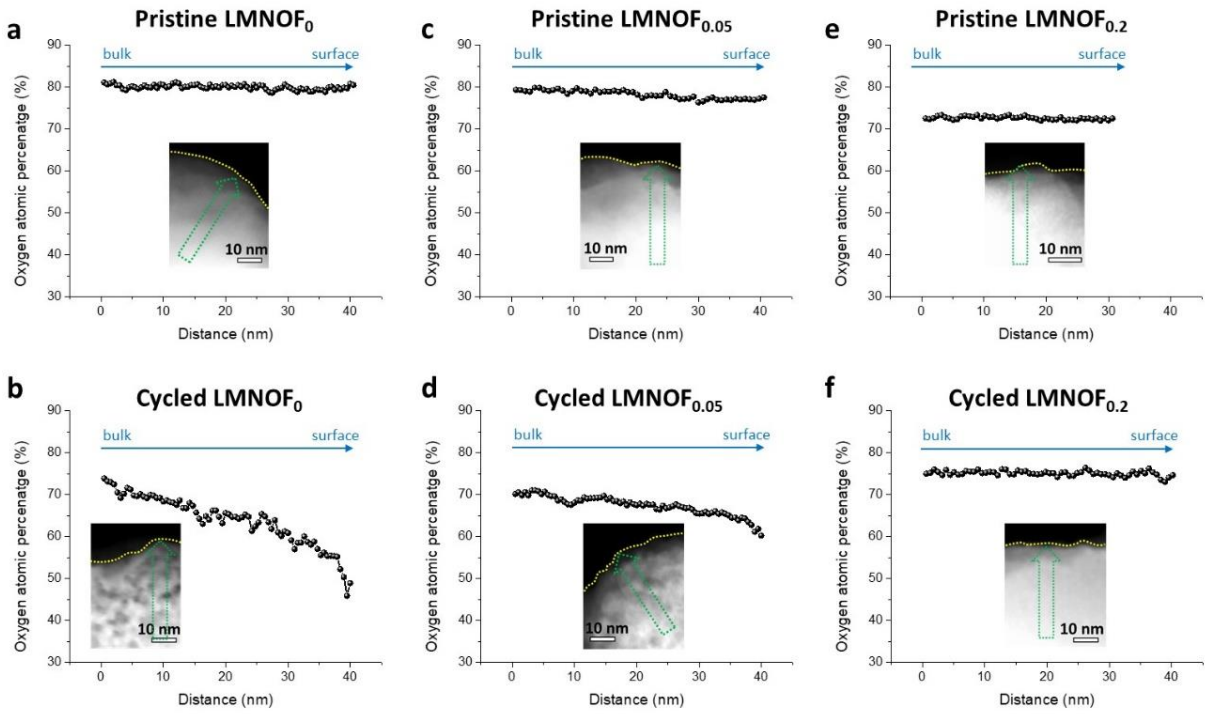

Figure 8. EELS linescan measurements of O concentration profile near the surface of (a) pristine $LMNOF_0$, (b) cycled $LMNOF_0$, (c) pristine $LMNOF_{0.05}$, (d) cycled $LMNOF_{0.05}$, (e) pristine $LMNOF_{0.2}$, and (f) cycled $LMNOF_{0.2}$ cathode particles. In the EELS measurements, only Mn and O are measured and quantified (the sum of the atomic percentages of Mn and O equals 100%), and only the O measurement data are plotted here.

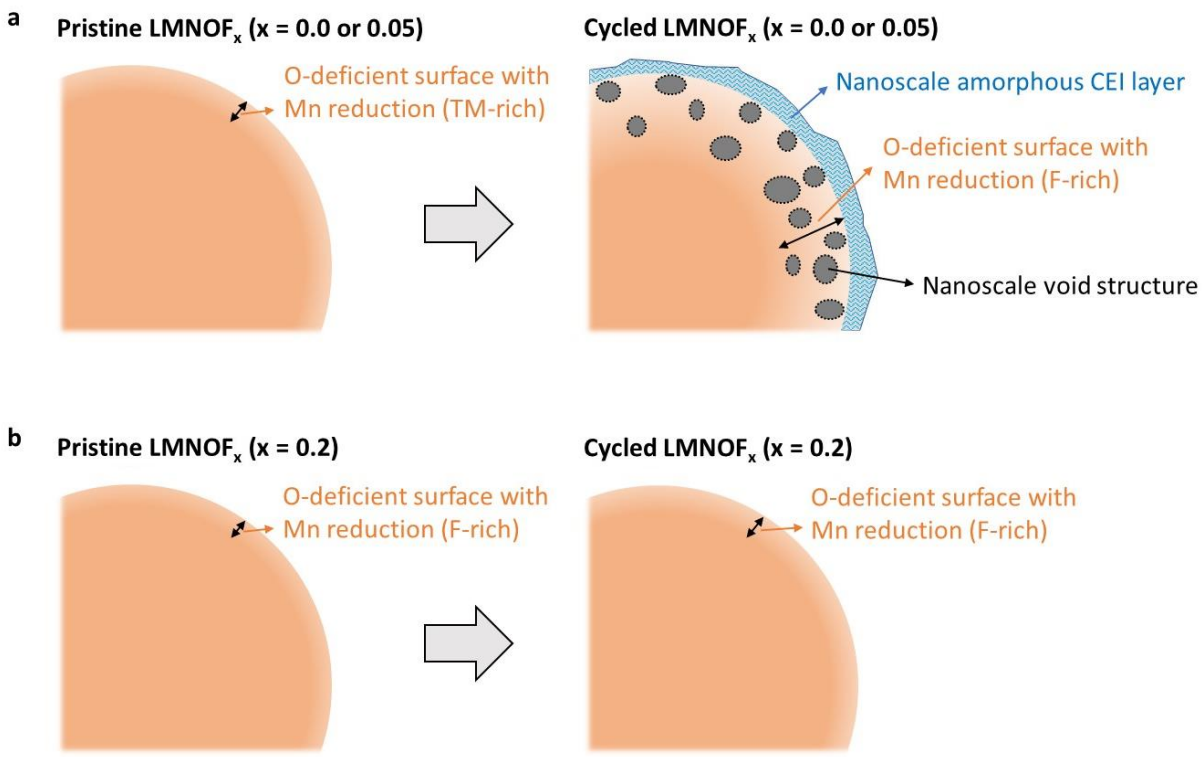

Figure 9. Schematics summarizing the observation of the structural and chemical evolutions in the $LMNOF_x$ cathode particles. (a) For the $LMNOF_x$ cathodes with zero or low F concentration (x = 0, 0.05), the cycling process leads to the formation of nanoscale amorphous CEI layers on the surface and void-like nanoregions featuring severe loss of O, Mn and Li at the subsurface, all of which can be detrimental to the Li transport. (b) For the $LMNOF_x$ cathodes with high F concentration (x = 0.2), the crystalline structure at the cathode surface and the stoichiometric elemental distribution at the subsurface is mostly well preserved after cycling, which ensures facile Li transport at the surface.